small methods
www.small-methods.com

Single-Step Patterning of Biocompatible Neural Electrodes Using Black-Pt Functionalized Laser-Induced Graphene for in Vivo Electrophysiology

*Giheon Kim, Yeonghwa Hong, Haeyun Lee, Minseok Kim, Jonghee Eun, Jimin Lee, Seungjun Lee, Namsun Chou, and Hyogeun Shin**

Neural electrodes are essential tools for monitoring electrophysiological activity in the brain, driving advances in neuroscience and neurotechnology. However, conventional semiconductor-based fabrication techniques suffer from high costs, complex procedures, and limited adaptability for customized designs. Here, a single-step patterning, scalable method is presented for fabricating biocompatible neural electrodes using laser-induced graphene (LIG) patterned directly onto polyimide substrates. This process requires only a standard CO_2 laser system, a spray-coated biocompatible lubricant, and black-Platinum (Pt) functionalization to form conductive traces, electrode sites, and connector pads—eliminating the need for cleanroom infrastructure or photolithography. Selective laser ablation enables precise electrode exposure, allowing rapid prototyping across various formats, including electroencephalography (EEG), electrocorticography (ECoG), and penetrating neural probes. The entire fabrication process is completed within 5 h, reducing production time and cost by over two orders of magnitude compared to conventional approaches. Demonstrating mechanical robustness, reliable signal acquisition, and biocompatibility, the fabricated electrodes exhibit high fidelity in recording EEG, ECoG, and spike signals in anesthetized mice. These findings underscore the method's strong potential for rapid prototyping of personalized brain-computer interfaces, neurological monitoring systems, and scalable preclinical research tools.

1. Introduction

The brain is a highly complex neural network composed of hundreds of billions of neurons that communicate via bioelectrical signals to form intricate neural circuits.[1,2] These circuits rely on electrochemical transmission across synapses and serve as fundamental mechanisms for regulating essential brain functions such as cognition, emotion, and motor control. In neuroscience, understanding the dynamics of these neural circuits is crucial for uncovering the mechanisms underlying human behavior and neurological disorders.[3] Neural electrodes are indispensable tools for detecting and recording subtle electrical signals generated in the brain, enabling real-time monitoring and precise analysis of neural activity.[4] In particular, neural signal acquisition through these electrodes plays a central role in a wide range of medical and engineering applications, including the diagnosis and treatment of neurological diseases and the development of brain-computer interfaces (BCIs).

G. Kim, H. Lee, M. Kim, S. Lee, H. Shin
School of Electronic and Electrical Engineering
College of IT Engineering
Kyungpook National University
Daegu 41566, Republic of Korea
E-mail: hyogeunshin@knu.ac.kr

The ORCID identification number(s) for the author(s) of this article can be found under https://doi.org/10.1002/smtd.202501384

DOI: 10.1002/smtd.202501384

Y. Hong, H. Shin
School of Electronics Engineering
College of IT Engineering
Kyungpook National University
Daegu 41566, Republic of Korea

J. Eun, J. Lee, S. Lee, N. Chou
Emotion, Cognition & Behavior Research Group
Korea Brain Research Institute (KBRI)
Daegu 41062, Republic of Korea

J. Lee
Department of Robotics and Mechatronics Engineering
Daegu Gyeongbuk Institute of Science and Technology (DGIST)
Daegu 42988, Republic of Korea

Current neural electrode technologies have evolved into several formats, including: 1) Silicon (Si)-based neural probes and micro-electrocorticography (micro-ECoG) arrays fabricated using semiconductor processes;[5,6] 2) flexible printed circuit board (FPCB)-based interfaces utilizing soft substrates;[7–9] and 3) electrode interfaces incorporating biocompatible conductive polymers such as poly(3,4-ethyleneoxythiophene):polysthyrene sulfonate (PEDOT:PSS) and polypyrrole (PPy).[10,11] Among these, semiconductor-fabricated electrodes offer high-density integration enabled by fine patterning, along with excellent mechanical stability and biocompatibility. These features have made them widely adopted in both clinical and preclinical research.[6,12,13] However, their fabrication requires cleanroom facilities and costly equipment, such as aligners, evaporators, sputtering systems, and reactive ion etchers (RIE), resulting in high capital investment (e.g., ≈$3 million for facility setup) and high unit costs ($500–1500 per electrode). Moreover, designing electrodes with specific functionalities or geometries demands additional photomasks and process modifications, making customization for patient-specific or research-driven applications time-consuming and resource-intensive.[14,15] For instance, implantable neural probes often require different electrode sizes, lengths, and channel counts depending on the experimental model or application, such as drug efficacy monitoring.[16] The need for multiple fabrication steps also leads to extended production cycles of 2–3 weeks or more, limiting research throughput and flexibility. These constraints create an urgent demand for a fabrication method that allows for the rapid, low-cost, and user-friendly development of custom neural electrodes.

Laser-induced graphene (LIG) is an emerging carbon-based material created by the direct photothermal conversion of a polymer precursor (e.g., polyimide (PI), polymethyl methacrylate (PMMA), polyethylene terephthalate (PET)), typically using a CO_2 laser (wavelength ≈10.6 µm) or other laser sources with wavelengths from the UV to visible light.[17–22] By tuning laser parameters, multiple layers of conductive graphene can be generated, resulting in a biocompatible material with a high specific surface area (≈340 $m^2\ g^{-1}$) and excellent electrical conductivity (5–25 S cm^{-1}).[23,24] Unlike traditional semiconductor microfabrication, LIG enables direct patterning on a single material using a laser alone, eliminating the need for metal deposition, lithography, and etching. Owing to these advantages, LIG has seen growing use in biosensors, such as glucose and dopamine sensors, for point-of-care diagnostics and wearable sensors for electrophysiological signals such as Electroencephalography (EEG).[25–29] However, LIG-based electrodes reported to date often suffer from mechanical vulnerability; the graphene structures and signal lines are prone to damage under bending, friction, or mechanical stress, leading to signal degradation and reduced conductivity.[30,31] This limitation is especially problematic for implantable neural probes that operate in dynamic, mechanically active environments. To improve robustness, recent studies have explored encapsulating LIG electrodes with soft biocompatible materials like Polydimethylsiloxane (PDMS)[32] or liquid crystal polymers (LCPs).[31] However, these approaches typically involve complex procedures, such as polymer synthesis, coating, and curing, limiting their practical use to specific applications like Electrocardiogram (ECG) or Electromyogram (EMG) monitoring. Furthermore, for implantable neural electrodes, forming a stable insulating layer is essential to minimize electrical noise from surrounding tissues and suppress foreign body reactions (FBR).

In this study, we present a single-step patterning method for biocompatible neural electrodes based on laser-induced graphene (LIG), enabling the rapid production of Electroencephalography (EEG), Electrocorticography (ECoG), and implantable probes suitable for in vivo electrophysiology. This streamlined approach utilizes only a CO_2 laser and a spray-coated biocompatible lubricant, eliminating the need for cleanroom processes or complex lithography (Table S1, Supporting Information). Through direct laser irradiation, we pattern the entire electrode circuit—including recording sites, signal lines, and connector pads—into a graphene architecture on the polyimide substrate. We then apply a spray-coated lubricant to serve as a biocompatible insulating layer without the need for additional equipment or processing steps. A second, selective laser irradiation step removes the lubricant over the electrode regions, enabling controlled exposure of the recording sites. This fully laser-based, mask-free approach eliminates the need for conventional processes such as metal deposition, lift-off, and etching. The entire fabrication can be completed in just a few hours, allowing for the rapid development of custom electrode designs with varying geometries and channel configurations, tailored to specific experimental needs. The fabricated electrodes are validated in vivo through EEG, ECoG, and neural spike signal recordings in anesthetized mice. The electrodes also demonstrated cytocompatibility suitable for biological applications. The results confirm robust and stable signal acquisition across all electrode types, highlighting the potential of this approach for practical deployment in neuroscience research, clinical diagnostics, and future BCI systems.

2. Results

2.1. Fabrication of LIG-Based Neural Electrodes

Figure 1a,b illustrates the complete fabrication workflow for LIG-based neural electrodes using a single CO_2 laser system. As shown in Figure 1a, this approach enables the simultaneous production of three distinct types of neural electrodes—EEG, ECoG, and implantable neural probes—on a single polyimide (PI) substrate. This is achieved using only laser patterning and a biocompatible spray-coated lubricant, offering a streamlined and cost-effective alternative to conventional fabrication techniques. Especially, the method of spray-coating is suitable for high-resolution neural electrodes compared to other coating methods—stencil or screen printing—because of its precise alignment and conformal coating on 3D structure. By using a single-step patterning system for both electrode fabrication and insulation removal, submicron alignment was achieved without complex alignment procedures required for physical stencils. Also, a spray-coated layer provides a highly uniform and conformal encapsulation over the 3D topography of the LIG electrode.

Figure 1b details the six-step process: 1) A 50 µm-thick PI film is mounted onto a microscope glass slide (52 mm × 76 mm) using water-soluble double-sided tape. 2) Signal lines and connector pads are patterned via CO_2 laser irradiation. 3) A biocompatible lubricant is spray-coated to form the insulating layer, followed by thermal curing at 190 °C for 2 h. 4) Electrode sites are selectively

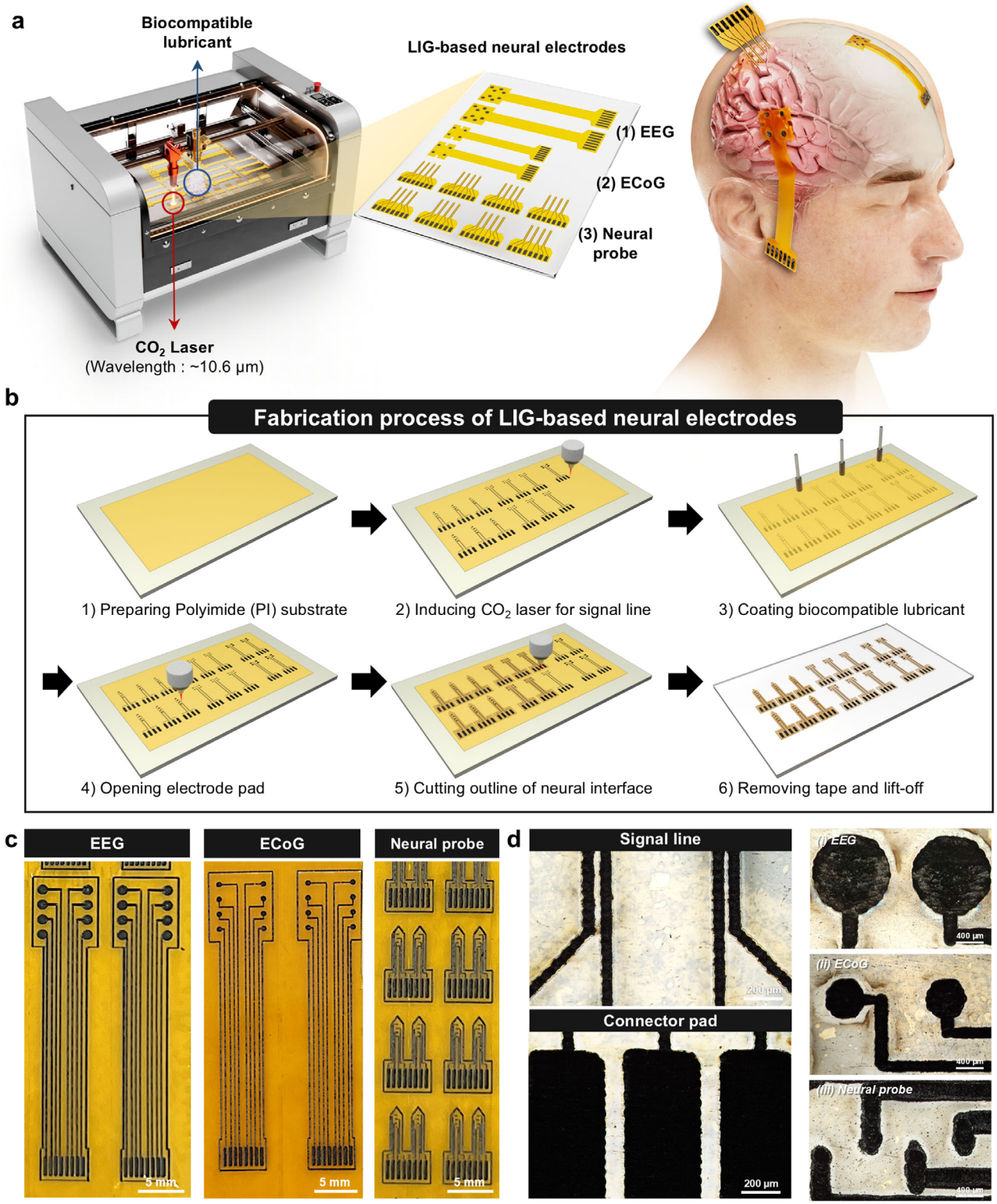

Figure 1. Schematic and fabrication process of LIG-based neural electrodes. a) Overview of the single-step laser fabrication process for producing LIG-based EEG, ECoG, and neural probe electrodes on a PI substrate. b) Step-by-step schematic of the fabrication process: 1) attachment of PI film using water-soluble tape, 2) laser patterning of signal lines and electrode pads, 3) spray coating of a biocompatible lubricant for insulation, 4) electrode re-opening via laser re-irradiation, 5) outline cutting, and 6) lift-off of the completed electrode. c) Photograph of the fabricated LIG-based neural electrodes, showing integration of all three electrode types on a single substrate. d) Magnified image of the electrode area, highlighting the fine laser-patterned signal lines and connector regions.

exposed by re-irradiating the laser with a multi-pass ablation process (two horizontal and two vertical sweeps) to completely remove the insulating layer from designated regions and reveal the underlying LIG surface. 5) The electrode outline is laser-cut to release the structure from the substrate. 6) The entire assembly is immersed in water for 1 h, dissolving the tape and yielding a freestanding, ready-to-use electrode. The use of water-soluble tape prevents thermal distortion of the PI film during laser exposure and enables clean, solvent-free lift-off (Movie S1 and Figure S1, Supporting Information).

This laser-based process offers a dramatic improvement over Micro-electromechanical system (MEMS)-based semiconductor fabrication, reducing total processing time to under 5 h and cutting production costs to as low as $0.04–$0.30 per device (Table S2 and Figure S2, Supporting Information). With fixed laser power and focus, only the scan speed needs to be adjusted, ensuring high reproducibility and scalability for various electrode configurations in a single fabrication run.

Fine patterning of signal lines is essential for high-density, multi-channel electrodes. To assess patterning resolution, scan speeds of 1, 5, 10, 20, 25, and 40 mm s^{-1} were tested. As scan speed increased, effective laser energy delivered to the substrate decreased, resulting in narrower line widths below 100 µm (Figure S3, Supporting Information). This exponential reduction in line width with scan speed provides precise control over electrode geometry and channel density (Figure S4, Supporting Information).

Using this versatile approach, we successfully fabricated functional EEG, ECoG, and neural probe devices (Figure 1c), each comprising signal lines, connector pads, and exposed electrode sites (Figure 1d).

2.2. Structural and Electrical Characteristics of the LIG Pattern

Figure 2a illustrates the structural configuration of the LIG-based neural electrode. The device consists of graphene-patterned signal lines and electrode sites formed on a PI substrate via laser irradiation. A biocompatible lubricant is applied to serve as an insulating layer. Electrode diameters were defined based on application: 1000 µm for EEG, 500 µm for ECoG, and 100 µm for neural probes.

As shown in the scanning electron microscopy (SEM) images in Figure 2b, both the signal lines and electrode sites were patterned precisely using a single laser process. High-magnification SEM images revealed a porous graphene network at the electrode sites. This porous morphology increases the effective surface area and enhances electrical conductivity, facilitating low-impedance neural signal acquisition. Figure 2c shows the surface appearance of the electrodes at different fabrication stages. The as-fabricated LIG appears dark due to carbonization. After coating with the biocompatible lubricant, the electrodes are covered by a white insulating film, clearly observable in both visual and SEM inspections. The primary role of the lubricant is to insulate the signal lines. As demonstrated in Figure S5 (Supporting Information), the coating is uniformly applied across the patterned structures. Elemental dispersive spectroscopy (EDS) analysis confirmed the presence of a Fluorine (F) signal from fluoropolymer-based lubricant coating graphene, verifying the formation of the insulating layer (Figures S6–S8, Supporting Information).

Upon laser re-irradiation to expose the electrodes, the insulating layer is completely removed, revealing the underlying LIG surface. Exposed electrode by lubricant removal led to applying post-black Pt deposition to further enhance the conductivity and sensitivity of the exposed LIG electrodes (Figure 2d; Figure S9, Supporting Information).

Raman spectroscopy was used to characterize the structural properties of the LIG patterns (Figure 2e). While the bare PI substrate showed minimal Raman signal, the LIG electrodes displayed prominent D (1350 cm^{-1}), G (1580 cm^{-1}), and 2D (2690 cm^{-1}) bands. The intensity ratio of the D to G bands (I_D/I_G) is a key indicator of structural defects and conductivity in graphene.[33] The pristine LIG exhibited an I_D/I_G ratio of 0.397, indicating low defect density and high crystallinity. After the electrode opening process, this ratio increased to 0.984, along with a more prominent 2D peak, suggesting increased porosity and improved charge storage capacity. These findings support the use of pristine LIG for signal lines and connector pads, while open LIG is better suited for high-sensitivity neural signal recording (Figure S10, Supporting Information).

Electrochemical performance was evaluated using electrochemical impedance spectroscopy (EIS) and cyclic voltammetry (CV), as shown in Figure 2f,g. For a 4 mm-diameter electrode, the pristine LIG exhibited an impedance of 3.14 ± 0.07 MΩ at 1 kHz. Upon applying the insulating layer, impedance increased more than tenfold to 35.1 ± 0.45 MΩ, confirming effective electrical isolation. After selective re-exposure of the electrode via laser, impedance dropped to 4.95 ± 0.01 MΩ, demonstrating restoration of electrical access (Figure 2f). Also, the sheet resistance was measured to characterize the electrical properties of the LIG electrode and the black Pt-coated electrode. The sheet resistance of the as-fabricated LIG electrode was measured to be 1.65 ± 0.15 kΩ sq^{-1}. After the black Pt electroplating, the sheet resistance significantly decreased to 0.93 ± 0.08 kΩ sq^{-1}. This reduction indicates that the highly conductive network was created onto the surface of the LIG electrode, contributing to the low electrical impedance of the electrode for various types of neural electrodes (Figure S11, Supporting Information). CV measurements under different scan rates further verified that the current density was significantly reduced after insulation and restored following electrode opening, confirming the preservation of electrochemical functionality (Figure 2g; Figure S12, Supporting Information).

Additionally, LIG-based electrodes are mechanically fragile under external stress, which can compromise signal stability.[30,31] To address this, we utilized the lubricant-based insulating layer to reinforce mechanical stability (Figure 2h,i). This was validated using both finite element analysis (FEA) and bending resistance tests.

FEA simulations indicated that stress in pristine LIG structures tends to concentrate at junctions between signal lines and electrodes. The presence of the lubricant significantly reduced strain in these critical regions (Figure 2h). To experimentally verify this, serpentine LIG patterns were fabricated and subjected to repeated bending under varying radii of curvature (0.01–0.1 mm^{-1}). Resistance measurements showed that pristine LIG structures exhibited up to an 843% increase in resistance due to mechanical failure, whereas lubricant-coated structures showed

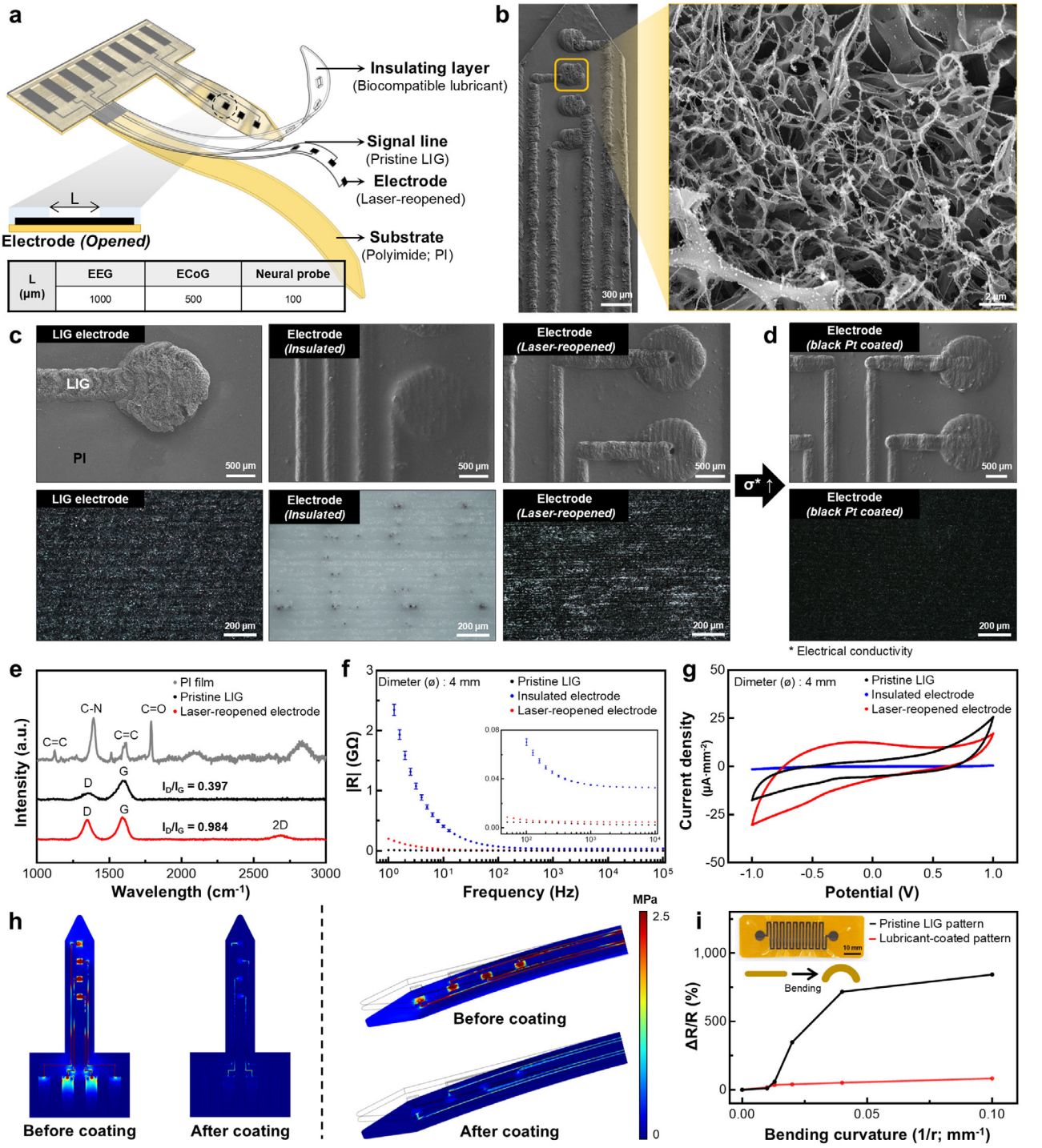

Figure 2. Structural and electrical characterization of the LIG pattern. a) Schematic of the LIG-based neural electrode structure, consisting of laser-patterned graphene signal lines and electrodes insulated with a spray-coated biocompatible lubricant. b) SEM images showing (top) the overall electrode and signal line structure, and (bottom) the porous graphene network at the electrode site. c) Optical and SEM images of the electrode surface at various fabrication stages: pristine LIG (left), lubricant-coated (middle), and laser-reopened electrode (right). d) SEM image of the electrode surface after black Pt electroplating. e) Raman spectra confirming the formation of graphene in the LIG electrode. Compared to the PI substrate, the laser-reopened LIG shows characteristic D (≈1350 cm^{-1}), G (≈1580 cm^{-1}), and 2D (≈2690 cm^{-1}) bands. f) Electrochemical impedance spectroscopy (EIS) of pristine, insulated, and laser-reopened LIG electrodes from 10^5 to 1 Hz. g) Cyclic voltammetry (CV) curves demonstrating changes in electrochemical activity before and after insulation and electrode reopening. h) Finite element analysis (FEA) simulation of mechanical stress in neural probes under bending, comparing uncoated and lubricant-coated structures. i) Relative resistance change of serpentine LIG electrodes under various bending curvatures, comparing pristine and lubricant-coated patterns. The data of EIS and relative resistance were presented as the mean ± standard deviation (SD); $n = 3$, where n is the number of samples.

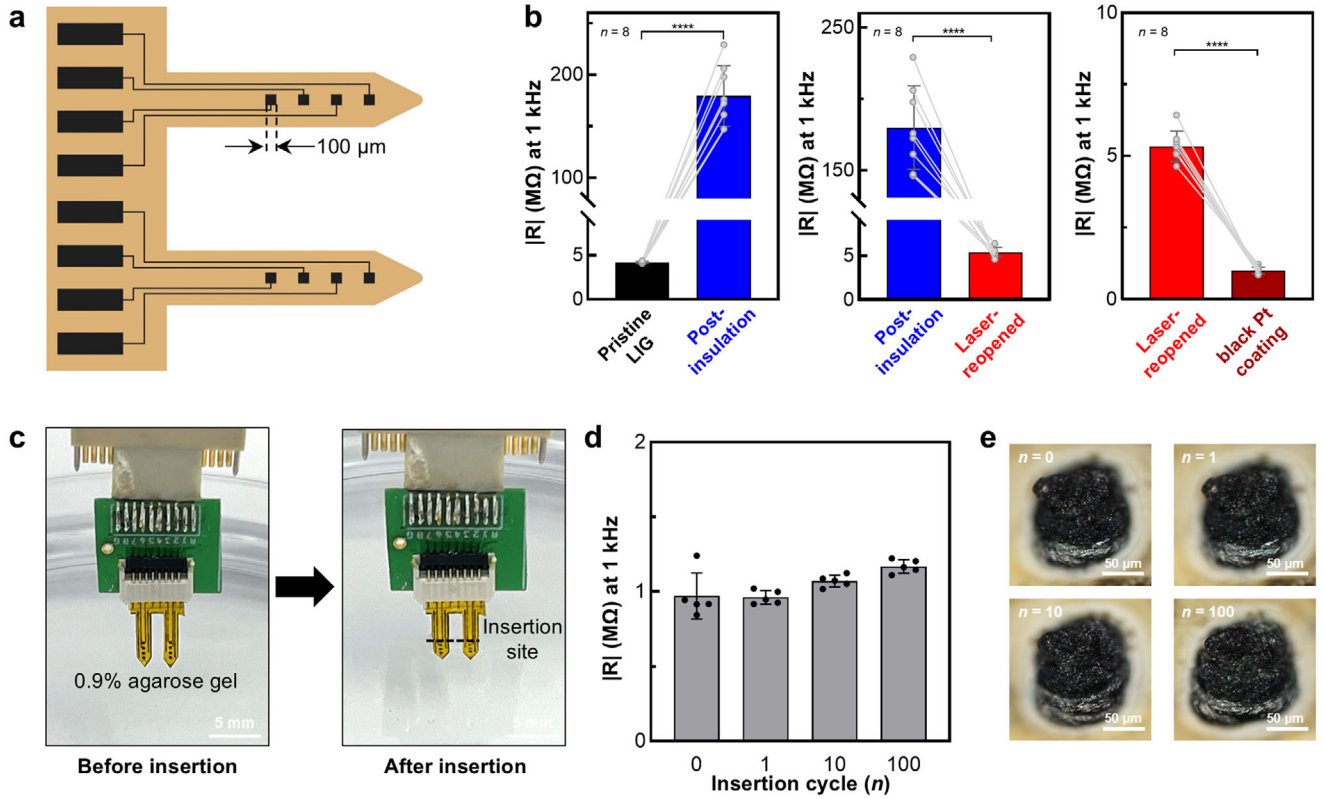

Figure 3. Electrical performance and mechanical durability of LIG-based neural electrodes. a) Schematic of the LIG-based neural probe. b) Impedance measurements (at 1 kHz) at key fabrication stages: pristine LIG, post-insulation, post-laser reopening, and after black Pt coating. The data were compared using a two-tailed unpaired student t-test: $t(14) = 16.86$, $p < 0.0001$ (pristine LIG vs post-insulation); $n = 8$, $t(14) = 10.85$, $p < 0.0001$ (post-insulation vs post-laser reopening); $n = 8$, $t(14) = 25.66$, $p < 0.0001$ (post-laser reopening vs black Pt coating); $n = 8$, where n is the number of neural probes. The data were presented as the mean ± standard deviation (SD). $^{****}p < 0.0001$. c) Impedance values recorded after 1, 10, and 100 repeated insertions of the neural probe into a 0.9% agarose brain phantom, confirming mechanical durability. d) Quantitative comparison of impedance increases across insertion cycles, showing minimal variation even after 100 insertions. The data were presented as the mean ± standard deviation (SD) with $n = 5$, where n is the number of neural probes after black Pt coating. e) Optical microscope images of the electrode before and after 100 insertions, confirming structural integrity with no delamination or breakage.

only ≈82% variation, confirming enhanced mechanical robustness (Figure 2i; Figures S13 and S14, Supporting Information).

In summary, we demonstrated that:

1) Laser-patterned LIG exhibits a porous, conductive structure suitable for use in signal lines and electrode sites.
2) The spray-coated biocompatible lubricant forms an effective, selectively removable insulating layer.
3) This insulating layer enhances both electrical isolation and mechanical durability.

These findings validate the proposed laser-based LIG fabrication platform as a simple, scalable, and robust strategy for neural interface development using a single material and fabrication tool.

2.3. Characteristics of the LIG-Based Neural Electrode

To assess the performance of the fabricated LIG-based neural electrodes, we evaluated their electrical properties, including electrode and signal line impedance, and the influence of the insulating layer under in vitro conditions (**Figure 3**; Figures S15 and S16, Supporting Information). Considering the frequency range of the signals being observed, impedance measurements were conducted at 1 kHz for neural probes and 10 Hz for EEG and ECoG electrodes.[34]

Figure 3b illustrates the impedance changes across each fabrication step for neural probe electrode sites. The pristine LIG electrode exhibited an impedance of 4.21 ± 0.11 MΩ at 1 kHz. Upon application of the insulating layer, impedance increased substantially to 179.58 ± 27.52 MΩ—approximately a 42-fold rise. Subsequent laser-assisted opening of the electrode site led to a reduction in impedance to 5.34 ± 0.49 MΩ, representing a high recovery of ≈79% of the pristine LIG impedance. Finally, electrochemical deposition of black Pt onto the opened electrode further reduced impedance to 1.00 ± 0.11 MΩ—an ≈179-fold reduction relative to the coated state—achieving levels well-suited for neural signal acquisition (Figure 3b).[35]

A comparable trend was observed for the EEG and ECoG electrodes. The initial impedance values for pristine LIG electrodes were 6.32 ± 0.95 MΩ for EEG and 7.58 ± 2.15 MΩ for ECoG at 10 Hz. After completing all processing steps, the final impedance values decreased to 563 ± 60 kΩ (EEG) and 750 ± 74 kΩ (ECoG), as shown in Figures S15 and S16 (Supporting

Information). These results confirm that the fabricated electrode sites exhibit sufficiently low impedance for effective neural signal detection. Additionally, the low standard deviations among samples indicate excellent process uniformity, supporting the scalability of this fabrication approach for large-scale production with high yield.

For neural probes, structural and electrical reliability under repeated insertion is critical. To evaluate mechanical durability, we conducted cyclic insertion and retraction tests using a 0.9% agarose gel brain phantom over 1, 10, and 100 cycles. After the first insertion, the electrode impedance was 962 ± 41 kΩ. Following 100 insertion cycles, impedance increased only slightly to 1.169 ± 0.04 MΩ, indicating negligible performance degradation and confirming robust durability (Figure 3c,d). Optical microscopy further revealed no visible structural damage, such as delamination of the electrode site or breakage of the signal lines, even after repeated mechanical loading (Figure 3e).

In summary, the fabricated LIG-based neural electrodes demonstrated both electrical stability and mechanical resilience during repeated use, establishing their reliability and reusability as a neural interface platform.

2.4. Cytocompatibility Assessment of LIG-Based Neural Electrodes

To evaluate the biocompatibility of the fabricated neural electrodes prior to in vivo application, cytotoxicity was assessed using the MTT assay with HepG2 cells. Two experimental conditions were tested: electrodes patterned with laser-induced graphene (LIG) alone, and electrodes coated with a biocompatible spray-type lubricant while maintaining the electrode sites exposed for signal transmission.

The results showed that cell viability remained above the commonly accepted 70% cytotoxicity threshold in both groups, indicating acceptable cytocompatibility, in accordance with ISO 10993–5 guidelines[36,37] (Figure S17, Supporting Information). Specifically, LIG-only samples exhibited a viability of 73.3 ± 10.6%, while samples with additional lubricant coating demonstrated improved viability of 90.7 ± 14.1%. This enhancement suggests that the insulating lubricant layer may help reduce the release of potentially reactive species into the culture medium, thereby improving the cytocompatibility of the device.

These findings confirm that the laser-based fabrication process and the materials used do not exert significant cytotoxic effects, supporting the suitability of the electrodes for neural interfacing. Moreover, the simplicity of the process—requiring no wet chemistry or harsh reagents—offers an inherently benign fabrication approach compatible with biological applications.

2.5. In Vivo Validation of LIG-Based Neural Electrodes

To assess the preclinical performance of the LIG-based neural electrodes, in vivo experiments were conducted using each electrode type (Figure S18, Supporting Information). **Figure 4** shows EEG signals recorded from a mouse using an 8-channel LIG-based EEG array before and after anesthesia, demonstrating both the device's in vivo functionality and its ability to capture physiological brain signals (Figure S19, Supporting Information). The EEG electrodes were positioned on the surface of the skull, with each channel targeting a distinct brain region for real-time monitoring (Figure 4a).

As illustrated in Figure 4b, low-frequency rhythms and intermittent spikes were observed during anesthesia, indicating sustained brain activity. Immediately after euthanasia, these physiological signals rapidly diminished, leaving only background noise. Frequency-domain analysis confirmed that low-frequency spectral power was present during anesthesia but was absent post-euthanasia (Figure 4c,d). Quantitative comparisons of EEG signals before and after euthanasia revealed substantial reductions in peak-to-peak amplitude and power across all major frequency bands: delta (δ; 1–4 Hz), theta (θ; 4–8 Hz), alpha (α; 8–13 Hz), beta (β; 13–30 Hz), and gamma (γ; 30–50 Hz) (Figure 4e–j).

For ECoG recordings, the electrodes were configured in an 8-channel array and placed directly on the cortical surface to assess neural activity before and after euthanasia (**Figure 5a**; Figure S20, Supporting Information). Similar to EEG results, robust signals were detected during anesthesia, while signal amplitudes decreased markedly across all channels after euthanasia (Figure 5b). Frequency-domain analysis revealed statistically significant power reductions across most frequency bands, verifying the LIG-based ECoG electrodes' capacity to detect in vivo neural signals (Figure 5c–j). Although both EEG and ECoG signals exhibited similar attenuation trends, EEG signals had consistently weaker peak-to-peak amplitude (161 ± 1.11 mV) and signal-to-noise ratio (SNR) (23.03 ± 0.11 dB), compared to 600 ± 5.76 mV and 23.03 ± 0.11 dB, respectively, in ECoG due to signal attenuation by the skull. These observations validate that LIG electrodes can function effectively in both EEG and ECoG configurations, depending on anatomical placement and application requirements (Figure S21, Supporting Information).

To further demonstrate the system's ability to capture neural spikes at the cell level, in vivo spike recordings were performed using an LIG-based neural probe. The probe, equipped with an LIG electrode site, was carefully inserted into the CA1 region of the hippocampus with minimal tissue disruption to ensure accurate targeting (**Figure 6a**; Figure S22, Supporting Information). Upon stable placement, various spike signals with distinct waveforms and amplitudes were reliably recorded, indicating a high signal-to-noise ratio (Figure 6b). Clear spike waveforms were observed in the time domain, and spike clustering analysis enabled the classification of signals from multiple individual neurons (Figure 6c). Additionally, we conducted a performance comparison with a silicon (Si)-based neural probe. The Si-based neural probe was fabricated as described in a previous study[38] and coated with black Pt under the same conditions as the LIG probe, then inserted into the identical CA1 brain region (Figure S23, Supporting Information). The comparative recordings demonstrated that the black Pt-coated LIG-based neural probe exhibited performance comparable to that of the Si-based probe (Figure 6d,e; Figure S24, Supporting Information).

Collectively, these results confirm that LIG-based neural electrodes provide a versatile, high-resolution platform for recording neural activity across different anatomical levels—from skull-surface EEG and cortical-surface ECoG to deep-brain spiking activity. The system supports customizable geometries and electrode configurations, enabling adaptation to specific experimental or clinical requirements. This flexible technology holds strong

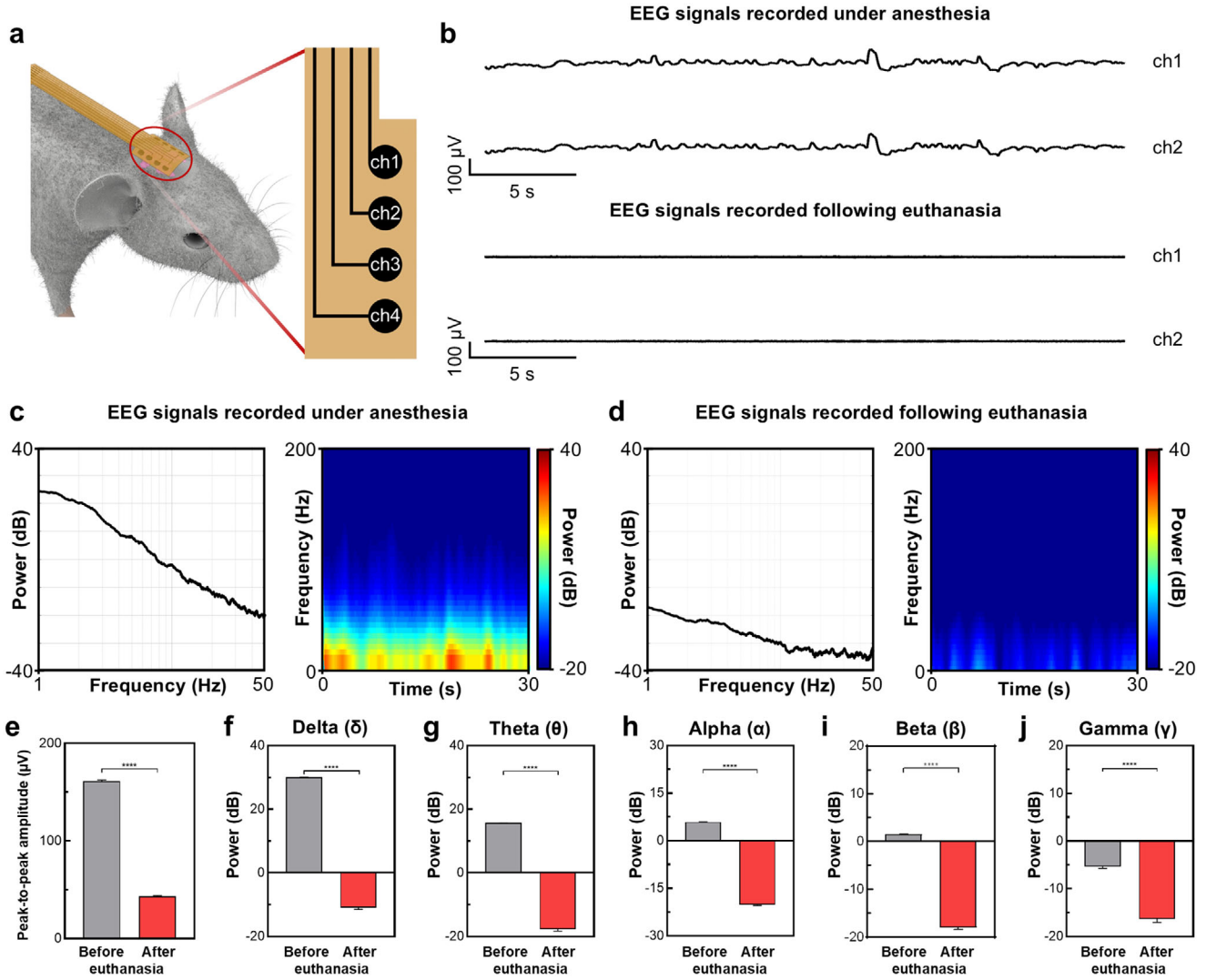

Figure 4. In vivo EEG recording using LIG-based neural electrodes. a) Schematic of the EEG recording setup with the LIG-based electrode array attached to the skull of an anesthetized mouse. b) Representative EEG signals recorded before (under anesthesia) and after euthanasia, showing the presence of low-frequency activity that disappears postmortem. c, d) Spectrogram analyses of EEG signals during anesthesia (c) and after euthanasia (d). e–j) Comparisons of peak-to-peak amplitude and power spectral density across frequency bands (δ, θ, α, β, and γ), illustrating significant reductions following euthanasia. The data were analyzed using a two-tailed unpaired student t-test: $t(6) = 155.9$, $p < 0.0001$ (peak-to-peak amplitude) $t(6) = 143.1$, $p < 0.0001$ (δ frequency), $t(6) = 110.7$, $p < 0.0001$ (θ frequency), $t(6) = 265.6$, $p < 0.0001$ (α frequency), $t(6) = 85.59$, $p < 0.0001$ (β frequency), $t(6) = 26.72$, $p < 0.0001$ (γ frequency); $n = 4$, where n is the number of electrodes that recorded signals. The data were presented as the mean ± standard deviation (SD). $^{****}p < 0.0001$.

potential for a wide range of applications, including diagnostics and therapeutic monitoring in neurological disorders.

3. Discussion

This study demonstrates that customizable LIG-based neural electrodes can be rapidly and efficiently fabricated using a single-step laser patterning process that relies on a single substrate and a single piece of patterning equipment. Leveraging the high electrical conductivity of LIG, implantable LIG electrodes were produced within 5 h without the need for photolithography or cleanroom facilities. Additionally, the use of a spray-coated biocompatible lubricant as an insulating layer not only provided effective electrical isolation between electrode sites and signal lines but also enhanced the mechanical robustness of the device. This insulating layer also improved the biocompatibility of the electrodes, as confirmed by MTT assays. As a result, the electrodes maintained stable impedance, reliable signal acquisition, and favorable biological compatibility, even under dynamic in vivo conditions.

The in vivo experiments confirmed that both EEG and ECoG electrodes were capable of capturing physiological brain signals across the full frequency spectrum. Moreover, the neural probe successfully detected spike signals, validating the LIG-based neural interface's capability to perform high-fidelity electrophysiological recordings at multiple anatomical levels,

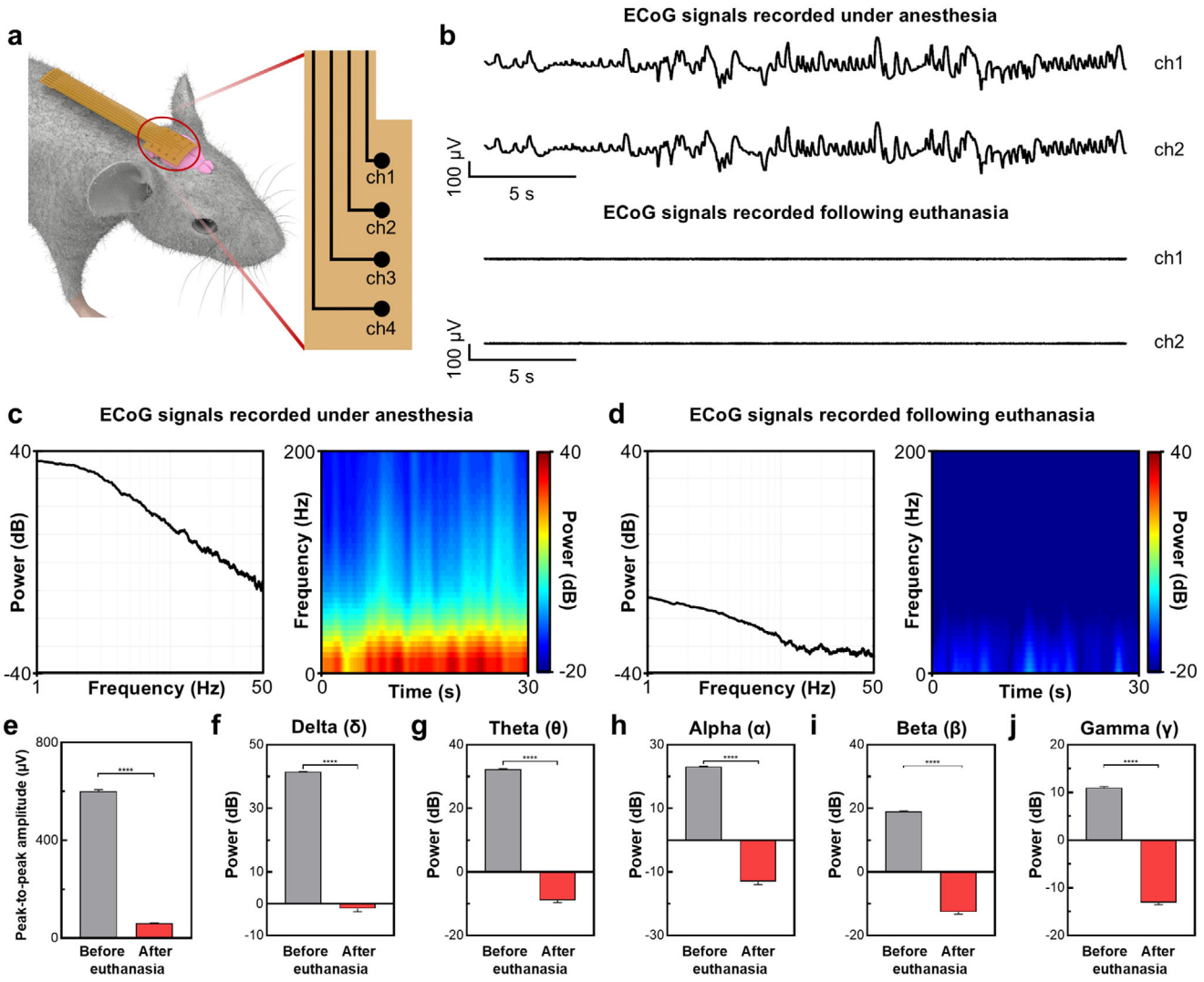

Figure 5. In vivo ECoG recording using LIG-based neural electrodes. a) Schematic of the ECoG recording setup, showing the LIG-based electrode array placed directly on the cortical surface following craniotomy. b) Representative ECoG signals from anesthetized and euthanized mice, indicating clear cortical activity during anesthesia and signal attenuation post-euthanasia. c, d) Spectrograms of ECoG signals during anesthesia (c) and after euthanasia (d). e–j) Quantitative comparisons of signal amplitude and frequency band power (δ, θ, α, β, and γ), confirming the physiological signal loss after death. The data were analyzed using a two-tailed unpaired student t-test: $t(6) = 158.5$, $p < 0.0001$ (peak-to-peak amplitude) $t(6) = 92.53$, $p < 0.0001$ (δ frequency), $t(6) = 99.13$, $p < 0.0001$ (θ frequency), $t(6) = 78.33$, $p < 0.0001$ (α frequency), $t(6) = 92.15$, $p < 0.0001$ (β frequency), $t(6) = 101.5$, $p < 0.0001$ (γ frequency). $n = 4$, where n is the number of electrodes that recorded signals. The data were presented as the mean ± standard deviation (SD). $^{****}p < 0.0001$.

including the skull surface, cortical surface, and deep brain regions.

One notable limitation of the current approach is the use of a CO_2 laser, which has a spot size of ≈100 μm. This restricts the fabrication of highly dense electrode arrays and narrow signal lines at sub-100 μm resolutions. However, recent advancements in UV laser technologies have enabled the creation of higher-resolution LIG patterns, offering a promising route to fabricate high-density neural electrode arrays in future iterations.[39]

The estimated cost per electrode using this fabrication strategy is ≈$0.04–0.30, underscoring its potential for low-cost, large-area BCIs, neural disorder monitoring platforms, and affordable neural probes for animal studies. Looking forward, integration with multi-channel wireless systems and electrical stimulation components could enable the development of next-generation, personalized closed-loop neuromodulation devices with strong translational potential.

4. Experimental Section

Preparation of LIG Patterns: LIG-based neural electrodes were fabricated by irradiating 50 μm-thick PI films using a CO_2 laser system (wavelength: 10.6 μm; beam diameter: 100 μm; maximum power: 40 W; model: ML-3040, Korea). The laser power was optimized to ≈4.7 W, with different scan rates applied to individual functional regions for precise patterning. Specifically, scan rates were set to 50 mm s^{-1} for electrode

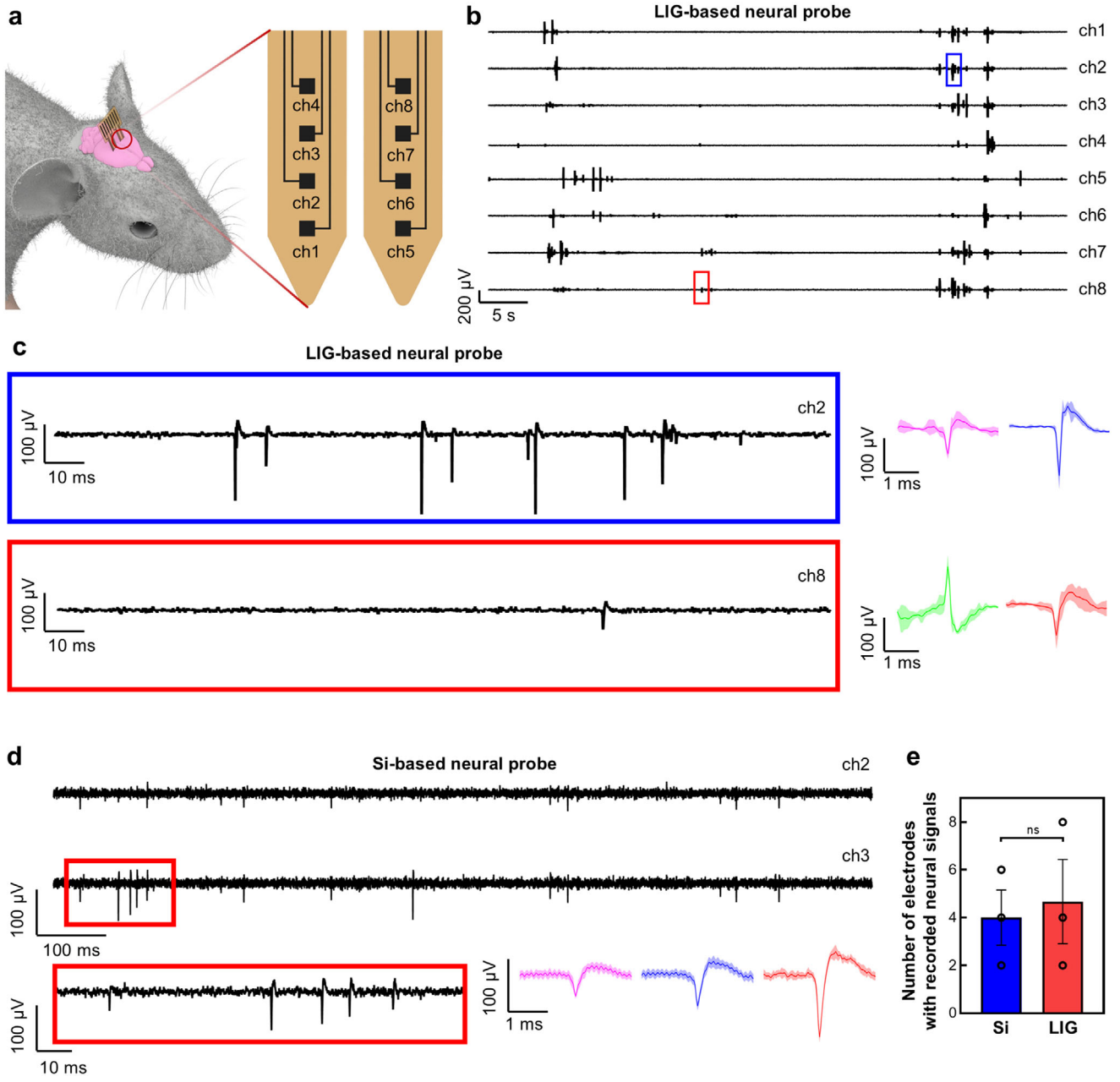

Figure 6. In vivo spike recording using a LIG-based neural probe. a) Schematic illustrating insertion of the LIG-based neural probe into the mouse brain for single-unit recordings. b) Representative raw spike traces acquired from the LIG-based neural probe. c, d) Time-domain plots of spike waveforms extracted from individual neurons using the LIG-based and Si-based neural probes. e) Comparison of the number of electrodes that recorded neural signals between the LIG-based and Si-based probes. The data were analyzed using a two-tailed unpaired Student's t-test: $t(4) = 0.3162$, $p = 0.7676$. $n = 3$, where n is the number of mice. The data were presented as the mean ± standard deviation (SD). ns $p > 0.05$.

regions, 80 mm s^{-1} for signal traces, 75 mm s^{-1} for connector pads, and 45 mm s^{-1} for the device outline.

Fabrication of LIG-Based Neural Electrodes: Three types of neural electrodes—EEG, ECoG, and penetrating neural probes—were designed using AutoCAD and patterned via CorelLASER software. The 50 µm-thick PI film was fixed onto a 52 mm × 76 mm glass slide using water-soluble double-sided tape. Sequential CO_2 laser processing was then used to define 1) signal lines, 2) connector pads, 3) electrode sites, and 4) the outer device boundary.

To electrically insulate the conductive regions and improve mechanical stability, a biocompatible lubricant (LYNK Solution, LYNK SOLUTEC, Korea) was spray-coated over the entire patterned surface. The substrate was thermally cured in an oven at 190 °C to solidify the insulating layer. After curing, selective laser re-irradiation was performed to remove the insulating layer from the electrode sites, thereby re-exposing them for signal transduction.

To enhance the sensitivity of neural signal acquisition, black Pt was electroplated onto the exposed LIG electrode sites. The plating

solution was prepared by dissolving 8% (w/v) hexachloroplatinic acid hydrate (H_2PtCl_6), 0.025% (w/v) lead(II) acetate, and 35% hydrochloric acid in deionized water.[38] The LIG electrodes acted as the working electrode (WE) and were immersed in the plating bath. A constant potential of 200 mV was applied for 120 s versus a Pt wire counter electrode (CE) and an Ag/AgCl reference electrode (RE), using a NanoZ system (White Matter LLC, USA).

Fabricated neural electrodes were connected to a printed circuit board (PCB) to acquire a neural signal. A 0.3 mm-thick tape was adhered to the backside of the PI substrate, specifically at the contact pad area, to enhance local stiffness, to distribute contact pressure, and to improve handling.

Characterization of the LIG Pattern—Morphological Characterization: The surface morphology of the LIG patterns and electrode structures was analyzed using an optical microscope (Nikon, Japan) and a field-emission scanning electron microscope (FE-SEM, SU-8230, Hitachi), operated at an accelerating voltage of 10 kV with a working distance of 8 mm.

Characterization of the LIG Pattern—Structural Characterization: Elemental composition and spatial distribution were assessed via EDS using an X-max80 EDS detector (Oxford Instruments) integrated with the FE-SEM. Both pristine and insulating layer-coated LIG electrodes were evaluated. Raman spectroscopy (inVia Reflex, Renishaw) was used to confirm graphene formation, employing a 532 nm excitation laser and scanning the spectral range of 1000–4000 cm^{-1}.

Characterization of the LIG Pattern—Electrical Characterization: The electrical properties of the LIG electrodes were assessed at three fabrication stages: i) pristine, ii) after insulation coating, and iii) after laser re-opening. EIS and CV were conducted using a PalmSens4 potentiostat (PalmSens). For EIS, 4 mm-diameter LIG samples were used as the working electrode, with a Pt wire as the counter electrode and an Ag/AgCl reference electrode. Measurements were performed in 1× phosphate-buffered saline (PBS) across a frequency range of 10^5–1 Hz with an excitation voltage of 100 mV. CV tests were performed in the same electrolyte from −1.0 to +1.0 V versus Ag/AgCl, at scan rates of 1000, 500, 100, 50, and 10 mV s^{-1}.

Characterization of the LIG Pattern—Mechanical Durability (Bending Resistance): The mechanical durability of the LIG electrodes under bending stress was evaluated by measuring resistance changes at varying radii of curvature (1/r). Controlled bending was applied using custom 3D-printed fixtures with defined radii of 100, 75, 50, 25, and 10 mm.

Characterization of the LIG-Based Neural Electrodes—Bending Stress Simulation: Finite element analysis (FEA) was conducted using COMSOL Multiphysics to simulate the bending deformation of the neural probe. A uniform pressure of 30 kPa was applied to both lubricant-coated and uncoated versions of the 4-channel LIG-based neural probe to assess the mechanical protection offered by the insulating layer. The simulation focused on evaluating the layer's effectiveness in mitigating stress-induced deformation and preventing delamination of the underlying graphene structure.

Characterization of the LIG-Based Neural Electrodes—Electrochemical Impedance Analysis: The electrochemical behavior of the LIG-based neural electrodes—EEG, ECoG, and neural probes—was characterized using the NanoZ impedance analysis system (White Matter LLC, USA). EIS was conducted for four distinct electrode conditions: pristine LIG, insulating layer-coated LIG, laser-reopened LIG, and black Pt-coated LIG. In each case, the LIG electrode functioned as the working electrode (WE), with an Ag/AgCl electrode as the reference, in a 1× PBS electrolyte. For EEG and ECoG electrodes, impedance was measured at 10 Hz to reflect their typical operational frequency range. For neural probes, measurements were performed at 1 kHz to match the frequency range relevant to high-resolution spike recordings.

Characterization of the LIG-Based Neural Electrodes—Insertion Testing: To evaluate the mechanical and electrical durability of the LIG-based neural probe, repeated insertion tests were performed using a brain tissue-mimicking hydrogel composed of 0.9% agarose. The probe was inserted and retracted through the gel across four cycle counts (n = 0, 1, 10, and 100). After each set of insertions, impedance measurements were recorded using the NanoZ system. Additionally, the electrode surface morphology was monitored before and after the tests via optical microscopy to assess any physical damage or degradation due to repeated mechanical stress.

MTT Assay for Cytotoxicity Evaluation: To evaluate the cytocompatibility of the fabricated electrodes, an MTT assay was conducted by KMED-Hub Tech (Daegu, South Korea) using HepG2 cells. Two experimental conditions were tested: 1) samples with only laser-induced graphene (LIG) patterning, and 2) samples coated with a biocompatible lubricant for electrical insulation, with the electrode sites selectively left open to reflect the intended in vivo application. For each condition, the samples were immersed in DMEM supplemented with 10% fetal bovine serum and incubated at 37 °C for 3 days to allow material conditioning. The conditioned media were then collected and applied to HepG2 cells cultured in 96-well plates. After incubation for up to 2 days, cell viability was assessed using the MTT assay, and absorbance was measured at 450 nm using a microplate reader. All values were normalized to the control group treated with unconditioned medium.

In Vivo Electrophysiological Experiments: All animal procedures were approved by the Korea Brain Research Institute (KBRI; Daegu, Korea) and conducted in accordance with institutional ethical guidelines set by the KBRI Animal Care and Use Committee. Male C57BL/6 mice (10 weeks old, ≈25 g) were used for all procedures. Mice were anesthetized with an intraperitoneal injection of 0.5% urethane (400 mg kg^{-1} body weight) and secured in an automated stereotaxic frame (71 000 Automated Stereo Instrument, RWD Life Science, USA).

Following a midline scalp incision, the skull was exposed to facilitate electrode placement. Electrode positioning (EEG, ECoG, and neural probe) was guided by stereotaxic coordinates derived from the Paxinos and Franklin mouse brain atlas.[40] For EEG recordings, the LIG-based electrode array was affixed directly to the intact skull using a biocompatible adhesive. For ECoG and spike recordings, burr holes were carefully drilled using a microdrill. The ECoG electrode was positioned beneath the skull, in direct contact with the dura mater, while the neural probe was stereotaxically inserted into a specific brain region. In all configurations, a reference screw was implanted in the cerebellum to serve as the reference electrode.

EEG and ECoG Signal Acquisition and Analysis: Neural signals were recorded from anesthetized mice implanted with LIG-based EEG and ECoG electrodes. For EEG, the electrode array was fixed onto the skull surface using biocompatible adhesive, without any surgical removal of the bone. For ECoG, a portion of the skull was removed using a microdrill to expose the cortical surface, and the electrode was placed directly onto the brain, without penetrating the dura.

All neural signals were acquired using the RHD2000 data acquisition system (Intan Technologies, USA) via the RHX software interface. Recordings were sampled at 20 kS s^{-1} per channel, digitized with a 16-bit analog-to-digital converter (ADC), and band-pass filtered (0.1 Hz high-pass, 6 kHz low-pass). Continuous recordings were maintained for at least 5 min while animals remained under anesthesia.

Post-processing and signal analysis were performed in MATLAB (MathWorks, USA). Frequency components were extracted using FFT-based spectrogram analysis. Special attention was given to delta (1–4 Hz) and theta (4–8 Hz) bands, which are dominant under anesthetic conditions. Power spectral density (PSD) plots and spatial heatmaps were generated to visualize neural signal power and regional activity distributions. SNR was calculated as described previously:[29,41]

$$\mathrm{SNR}\ (\mathrm{dB}) = 20\log 10\frac{A_s}{A_n} \quad (1)$$

where A_s is the highest signal peak of the neural signal and A_n is the standard deviation (SD) of the background noise.

Preparation and Characterization of Si-based Neural Probe: To evaluate the performance of the LIG-based neural probe, a comparison with a Si-based neural probe was conducted. The Si-based probe was fabricated as described previously[38] and consisted of eight electrode sites (19 × 19 µm each) with a probe thickness of 40 µm and a width of 85 µm. The fabricated Si probe was mounted on a custom PCB, followed by wire bonding and

connector attachment to enable stable electrical interfacing. To enhance signal recording performance, the electrode sites were electroplated with black Pt. The impedance of the Si electrodes was measured as 1.54 ± 0.3 MΩ before coating, which was reduced to 38.3 ± 22.5 kΩ after black Pt deposition. Both the plating and impedance measurements were performed using the same protocols as applied for the LIG-based neural electrodes.

Spike Signal Recording and Analysis: To record single-unit spike activity from the hippocampus, the LIG-based neural probe and the Si-based neural probe were stereotaxically inserted into the CA1 region of anesthetized mice. The insertion coordinates were based on the Paxinos and Franklin mouse brain atlas: mediolateral (ML) = −1.5 mm, anteroposterior (AP) = −1.5 mm, and dorsoventral (DV) = −2.0 mm. After exposing the skull and dura, a burr hole was carefully drilled at the target site. The probe was then slowly lowered into the brain using an automated stereotaxic instrument to minimize tissue damage.

Neural activity was recorded using the RHD2000 data acquisition system (Intan Technologies, USA) via the RHX software interface. Signals were sampled at 20 kS s^{-1} per channel, band-pass filtered using a 300 Hz high-pass and 6 kHz low-pass filter, and digitized with a 16-bit ADC. Continuous recordings were maintained for a minimum of 5 min under anesthesia.

Spike analysis was conducted using a MATLAB-based spike sorting algorithm, as previously described.[38] Spike events were detected when their amplitudes exceeded a threshold of twice the baseline noise level (≈30 µV). Extracted spike waveforms were visualized using raster plots, and subsequent spike sorting and clustering confirmed the presence of distinct, neuron-specific firing patterns. These results demonstrated that the LIG-based neural probe was capable of reliably detecting single-unit activity from deep brain structures with a high signal-to-noise ratio (SNR).

Statistical Analysis: All statistical analyses were performed using GraphPad Prism 8 (GraphPad Software). No specific pre-processing steps, such as transformation or normalization, were applied to the data. All quantitative data are presented as the mean ± standard deviation (SD). The sample size (n) for each experiment, representing the number of independent samples, is indicated in the respective figure legends.

Student's *t*-test was used to determine statistical significance between two groups. A P value of less than 0.05 was considered statistically significant. Significance levels are denoted in the figures as follows: *ns*, $p > 0.05$; $^{***}p < 0.001$; $^{****}p < 0.0001$.

Supporting Information

Supporting Information is available from the Wiley Online Library or from the author.

Acknowledgements

This work was supported by the Technology Innovation Program (RS-2025-04812973, Neuro-Semi-AI Fusion Superhuman Project: A Platform for Augmenting Physical Abilities Based on Central Nervous System Stimulation) funded by the Ministry of Trade, Industry & Energy (MOTIE, Korea). This work was supported by the National Research Foundation of Korea (NRF) grant funded by the Korean government (MSIT) (RS-2025-00557203). This research was supported by the Bio&Medical Technology Development Program of the National Research Foundation (NRF) funded by the Korean government (MSIT) (RS-2025-02243041). This work was supported by the Innovative Human Resource Development for Local Intellectualization program through the Institute of Information & Communications Technology Planning & Evaluation (IITP) grant funded by the Korea government (MSIT) (IITP-2025-RS-2022-00156389). This work has also been supported by the Korea Brain Research Institute research program funded by the Ministry of Science and ICT (25-BR-02-02, 25-BR-04-01).

Conflict of Interest

The authors declare no conflict of interest.

Author Contributions

G.K. did data curation, methodology, resources, software, formal analysis, investigation, validation, visualization, and writing of the original draft. Y.H. did data curation and methodology. H.L. did methodology. M.K. did the methodology. J.E. did resources. J.L. did resources. S.L. did resources. N.C. did resources and funding acquisition. H.S. did conceptualization, methodology, resources, software, validation, formal analysis, writing of the review & editing, visualization, supervision, project administration, and funding acquisition.

Data Availability Statement

The data that support the findings of this study are available from the corresponding author upon reasonable request.

Keywords

flexible neural electrode, high-throughput fabrication, in vivo electrophysiology, laser-induced graphene (LIG), neural interface

Received: July 15, 2025
Revised: September 8, 2025
Published online: September 18, 2025

[1] F. A. C. Azevedo, L. R. B. Carvalho, L. T. Grinberg, J. M. Farfel, R. E. L. Ferretti, R. E. P. Leite, W. J. Filho, R. Lent, S. Herculano-Houzel, *J. Comparative Neur.* **2009**, *513*, 532.
[2] G. Hahn, A. Ponce-Alvarez, G. Deco, A.d Aertsen, A. Kumar, *Nat. Rev. Neurosci.* **2019**, *20*, 117.
[3] T. N. Lerner, L. Ye, K. Deisseroth, *Cell* **2016**, *164*, 1136.
[4] K. Woeppel, Q. Yang, X. T. Cui, *Curr. Opin. Biomed. Eng.* **2017**, *4*, 21.
[5] B. Rubehn, C. Bosman, R. Oostenveld, P. Fries, T. Stieglitz, *J. Neural Eng.* **2009**, *6*, 036003.
[6] J. J. Jun, N. A. Steinmetz, J. H. Siegle, D. J. Denman, M. Bauza, B. Barbarits, A. K. Lee, C. A. Anastassiou, A. Andrei, Ç. Aydin, M. Barbic, T. J. Blanche, V. Bonin, J. Couto, B. Dutta, S. L. Gratiy, D. A. Gutnisky, M. Häusser, B. Karsh, P. Ledochowitsch, C. M. Lopez, C. Mitelut, S. Musa, M. Okun, M. Pachitariu, J. Putzeys, P. D. Rich, C. Rossant, W.-L. Sun, K. Svoboda, et al., *Nature* **2017**, *551*, 232.
[7] H. Lee, S. Park, M. Kim, J. Lee, S. Lee, N. Chou, H. Shin, *Sens. Actuat. A* **2025**, *387*, 116437.
[8] H. Lee, S. Lee, S. Lee, J. Lee, N. Chou, H. Shin, *ACS Omega* **2025**, *10*, 10733.
[9] M. Kim, S. Park, H. Lee, J. Lee, N. Chou, H. Shin, *Adv. Electron. Mater.* **2025**, *11*, 2500121.
[10] R. Green, M. R. Abidian, *Adv. Mater.* **2015**, *27*, 7620.
[11] H. W. Kim, J. Kim, J. Y. Kim, K. Kim, J. Y. Lee, T. Kim, S. Cho, J. B. An, H. J. Kim, L. Sun, S. Lee, K. Fukuda, T. Someya, M. Sang, Y. U.k Cho, J. E. Lee, K. J. Yu, *Nat. Commun.* **2025**, *16*, 4032.
[12] N. A. Steinmetz, C. Aydin, A. Lebedeva, M. Okun, M. Pachitariu, M. Bauza, M. Beau, J. Bhagat, C. Böhm, M. Broux, S. Chen, J. Colonell, R. J. Gardner, B. Karsh, F. Kloosterman, D. Kostadinov, C. Mora-Lopez, J. O'Callaghan, J. Park, J. Putzeys, B. Sauerbrei, R. J. J. van Daal, A. Z. Vollan, S. Wang, M. Welkenhuysen, Z. Ye, J. T. Dudman, B. Dutta, A. W. Hantman, K. D. Harris, et al., *Science* **2021**, *372*, abf4588.
[13] A. C. Paulk, Y. Kfir, A. R. Khanna, M. L. Mustroph, E. M. Trautmann, D. J. Soper, S. D. Stavisky, M. Welkenhuysen, B. Dutta, K. V. Shenoy, L. R. Hochberg, R. M. Richardson, Z. M. Williams, S. S. Cash, *Nat. Neurosci.* **2022**, *25*, 252.
[14] S. R. Patel, C. M. Lieber, *Nat. Biotechnol.* **2019**, *37*, 1007.

[15] M. Zhang, Z. Tang, X. Liu, J. Van der Spiegel, *Nat. Electron.* **2020**, *3*, 191.
[16] Y. Yoon, H. Shin, D. Byun, J. Woo, Y. Cho, N. Choi, I.l-J. Cho, *Nat. Commun.* **2022**, *13*, 5521.
[17] W. Gao, N. Singh, L.i Song, Z. Liu, A. L. M. Reddy, L. Ci, R. Vajtai, Q. Zhang, B. Wei, P. M. Ajayan, *Nat. Nanotechnol.* **2011**, *6*, 496.
[18] R. Ye, D. K. James, J. M. Tour, *Acc. Chem. Res.* **2018**, *51*, 1609.
[19] Q. Yang, L. Cao, S. Li, X. Zeng, W. Zhou, C. Zhang, *J. Anal. Appl. Pyrolysis* **2023**, *173*, 106074.
[20] M. Qu, Y. Guo, Y. Cai, Z. Nie, C. Zhang, *Small* **2024**, *20*, 2310273.
[21] Y. Guo, C. Zhang, Y.e Chen, Z. Nie, *Nanomaterials* **2022**, *12*, 2336.
[22] J. Lin, Z. Peng, Y. Liu, F. Ruiz-Zepeda, R. Ye, E. L. G. Samuel, M. J. Yacaman, B. I. Yakobson, J. M. Tour, *Nat. Commun.* **2014**, *5*, 5714.
[23] Z. Peng, J. Lin, R. Ye, E. L. G. Samuel, J. M. Tour, *ACS Appl. Mater. Interfaces* **2015**, *7*, 3414.
[24] R. Ye, D. K. James, J. M. Tour, *Adv. Mater.* **2019**, *31*, 1803621.
[25] A. F. Carvalho, A. J. S. Fernandes, C. Leitão, J. Deuermeier, A. C. Marques, R. Martins, E. Fortunato, F. M. Costa, *Adv. Funct. Mater.* **2018**, *28*, 1805271.
[26] N. F. Santos, S. O. Pereira, A. Moreira, A. V. Girão, A. F. Carvalho, A. J. S. Fernandes, F. M. Costa, *Adv. Mater. Technol.* **2021**, *6*, 2100007.
[27] J. Zhu, S. Liu, Z. Hu, X. Zhang, N. Yi, K. Tang, M. G. Dexheimer, X. Lian, Q. Wang, J. Yang, J. Gray, H. Cheng, *Biosens. Bioelectron.* **2021**, *193*, 113606.
[28] F. Amirghasemi, A. Al-Shami, K. Ushijima, M. P. S. Mousavi, *ACS Mater. Lett.* **2024**, *6*, 4158.
[29] Q. Zhang, M. Qu, X. Liu, Y. Cui, H. Hu, Q. Li, M. Jin, J. Xian, Z. Nie, C. Zhang, *Adv. Mater. Interfaces* **2023**, *10*, 2201735.
[30] Y. Lu, G. Yang, S. Wang, Y. Zhang, Y. Jian, L. He, T. Yu, H. Luo, D. Kong, Y. Xianyu, B.o Liang, T. Liu, X. Ouyang, J. Yu, X. Hu, H. Yang, Z. Gu, W. Huang, K. Xu, *Nat. Electron.* **2024**, *7*, 51.
[31] R. Park, D. H. Lee, C. S.u Koh, Y. W. Kwon, S. Y. Chae, C.-S. Kim, H. H.o Jung, J. Jeong, S. W. Hong, *Adv. Healthcare Mater.* **2024**, *13*, 2301753.
[32] Y. K. Shin, K. H. Kim, M. H. Seo, *Micro Nano Syst. Lett.* **2023**, *11*, 9.
[33] B. Ma, R. D. Rodriguez, A. Ruban, S. Pavlov, E. Sheremet, *Phys. Chem. Chem. Phys.* **2019**, *21*, 10125.
[34] G. Buzsáki, C. A. Anastassiou, C. Koch, *Nat. Rev. Neurosci.* **2012**, *13*, 407.
[35] K. A. Ludwig, N. B. Langhals, M. D. Joseph, S. M. Richardson-Burns, J. L. Hendricks, D. R. Kipke, *J. Neural Eng.* **2011**, *8*, 014001.
[36] F. Burkhardt, B. C. Spies, C. Wesemann, C. G. Schirmeister, E. H. Licht, F. Beuer, T. Steinberg, S. Pieralli, *Sci. Rep.* **2022**, *12*, 7391.
[37] I. Nedeljkovic, B. Z. Doulabi, M. Abdelaziz, A. J. Feilzer, R. A. M. Exterkate, S. Szafert, N. Gulia, I. Krejci, C. J. Kleverlaan, *Dent. Mater.* **2022**, *38*, 2052.
[38] H. Shin, Y. Son, U. Chae, J. Kim, N. Choi, H. J. Lee, J. Woo, Y. Cho, S. H. Yang, C. J. Lee, I.l-J. Cho, *Nat. Commun.* **2019**, *10*, 3777.
[39] H. Lim, H. Kwon, H. Kang, J. E. Jang, H.-J. Kwon, *Nat. Commun.* **2023**, *14*, 3114.
[40] K. B. Franklin, in *The Mouse Brain in Stereotaxic Coordinates*, Academic Press, San Diego, USA **2001**.
[41] M. Ito, T. Horii, T. Fujie, *Adv. Mater. Interfaces* **2021**, *8*, 2100213.

